Applied Surface Science 276 (2013) 756–760

Contents lists available at SciVerse ScienceDirect

Applied Surface Science

journal homepage: www.elsevier.com/locate/apsusc

Using SiO_x nano-films to enhance GZO Thin films properties as front electrodes of a-Si solar cells

Kow-Ming Chang[a], Po-Ching Ho[b,*], Shu-Hung Yu[b], Jui-Mei Hsu[c], Kuo-Hui Yang[c], Chin-Jyi Wu[c], Chia-Chiang Chang[c]

[a] Electronics Engineering Dept., National Chiao Tung University; College of Electrical and Information Engineering, I-Shou University, Republic of China
[b] Department of Electronics Engineering & Institute of Electronics, National Chiao Tung University, 1001 Ta Hsueh Road, Hsinchu, Taiwan 30010, Republic of China
[c] Industrial Technology Research Institute, Mechanical and Systems Research Laboratories, 195, Sec. 4, Chung Hsing Rd., Chutung, Hsinchu, Taiwan 31040, Republic of China

ARTICLE INFO

Article history:
Received 26 January 2013
Received in revised form 20 March 2013
Accepted 25 March 2013
Available online 1 April 2013

Keywords:
Atmospheric pressure plasma
Light-trapping effect
Transparent conductive oxide

ABSTRACT

One of the essential applications of transparent conductive oxides is as front electrodes for superstrate silicon thin-film solar cells. Textured TCO thin films can improve absorption of sunlight for an a-Si:H absorber during a single optical path. In this study, high-haze and low-resistivity bilayer GZO/SiO_x thin films prepared using an atmospheric pressure plasma jet (APPJ) deposition technique and dc magnetron sputtering. The silicon subdioxide nano-film plays an important role in controlling the haze value of subsequent deposited GZO thin films. The bilayer GZO/SiO_x (90 sccm) sample has the highest haze value (22.30%), the lowest resistivity (8.98×10^{-4} Ω cm), and reaches a maximum cell efficiency of 6.85% (enhanced by approximately 19% compared to a sample of non-textured GZO).
© 2013 Elsevier B.V. All rights reserved.

1. Introduction

Transparent conductive oxide (TCO) has attracted substantial attention because of high transparency in the visible region and low resistivity. One of the most important applications of TCO is as a textured front electrode for superstrate pin-type silicon thin-film solar cells [1–3]. Textured TCO thin films can enhance sunlight absorption for the hydrogenated amorphous silicon (a-Si:H) absorber during one optical path and further improve the cell efficiency because of the light-trapping effect. There are several types of TCO materials, including tin-doped indium oxide (ITO), fluorine-doped tin oxide (FTO), and zinc oxide doped with group III elements (AZO, GZO). For amorphous silicon thin-film solar cells, both AZO and GZO are suitable front electrode materials because of their easily modified surface morphologies. Compared with ITO and FTO, they also have higher hydrogen and silane (SiH_4) plasma resistance and lower cost. GZO has a higher transmittance than AZO in the near-infrared region [4] and better moisture resistance because gallium exhibits low reactivity to oxygen [5].

The morphologies of the TCO front contact strongly affect their haze value. Several deposition techniques have been used to prepare textured ZnO films [6–8]. In this study, rough silicon subdioxide (SiO_x) buffer layers were deposited using the atmospheric pressure plasma jet (APPJ) to modify the morphologies and to influence the optoelectronic properties of the sputtered GZO thin films. After post-annealing in vacuum, bilayer GZO/SiO_x thin films obtained better optoelectronic properties and improved the efficiency of an a-Si solar cell compared to a non-textured GZO single layer.

2. Experiment

Rough SiO_x thin films were deposited at 75 °C on 100 mm × 100 mm × 3.2 mm glass substrates (Taiwan Glass Industry Co.) using the APPJ deposition technique. Fig. 1a shows a schematic diagram of the APPJ deposition system. The APPJ deposition system is mainly composed of a high-voltage AC power supply, a plasma jet, a precursor bottle, a hot plate, and an x–y directional scan system. The plasma power and frequency were 450 W and 20 kHz, respectively. The distance between the plasma jet nozzle to the substrate was 15 mm. The scanning route is shown in Fig. 1b. The y-direction scan speed was fixed at 250 mm/s, and the pitch was fixed at 2 mm. Hexamethyl-disiloxane [(HMDSO), Alfa Aesar] was used as the precursor to deposit the SiO_x buffer layers. To obtain various surface roughnesses of SiO_x thin films, the argon carrier gas flow rate was set to vary at 30 sccm, 60 sccm, or 90 sccm, and the flow rate of the compressed dry air (CDA) main gas was set at 40 SLM. The thickness of the SiO_x nano-films was 10 nm,

* Corresponding author. Tel.: +886 921841971.
E-mail address: raymondsam.ee98g@nctu.edu.tw (P.-C. Ho).

0169-4332/$ – see front matter © 2013 Elsevier B.V. All rights reserved.
http://dx.doi.org/10.1016/j.apsusc.2013.03.165

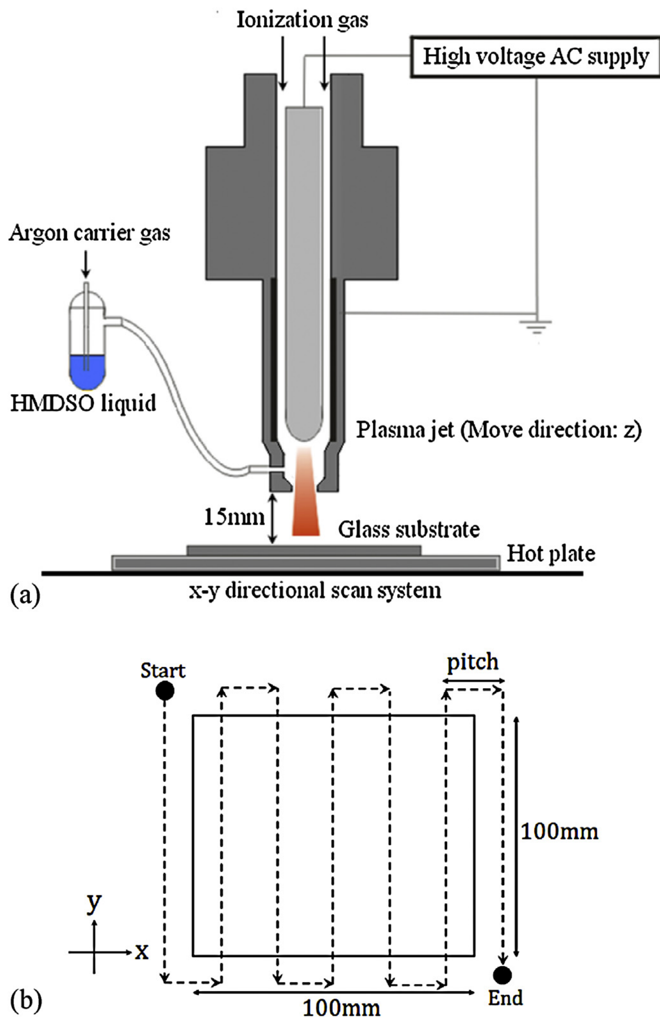

Fig. 1. Schematic diagram of (a) the APPJ deposition system and (b) the scanning route.

25 nm, and 30 nm for 30 sccm, 60 sccm, and 90 sccm, respectively. GZO thin films were deposited at 100 °C on SiO_x buffer layers using direct-current (DC) magnetron sputtering. A ceramic GZO target was doped with 3.2 wt.% Ga_2O_3. DC magnetron sputtering was performed at a working pressure of 2 mTorr in Ar working gas and at a DC power density of 3 W/cm^2. The thickness of the GZO thin films was 1 μm. All as-deposited bilayer GZO/SiO_x thin films were annealed in high vacuum (<1 × 10^{-6} Torr) at 500 °C for 5 min to improve adhesion between GZO and SiO_x thin films and remove chemisorbed oxygen ions on the surface of GZO thin films. Finally, the bilayer GZO/SiO_x thin films were applied to the amorphous silicon thin-film solar cells as a front electrode with the following structure: 3.2-mm-thick glass substrate/SiO_x buffer layers (10–30 nm)/GZO (1000 nm)/p-type a-Si:H (10 nm)/intrinsic a-Si:H absorber (300 nm)/n-type μc-Si:H (15 nm)/GZO (100 nm)/Ag (200 nm).

To investigate the surface morphologies of SiO_x and bilayer GZO/SiO_x films, a scanning electron microscope (Hitachi, S-4700I) was used. The X-ray diffraction (XRD; BRUKER, D2 PHASER) measurements were used to characterize the crystal orientation and quality of the films. The binding energy and chemical shift of the samples were measured using X-ray photoelectron spectroscopy (XPS). The electrical properties of bilayer GZO/SiO_x thin films and sputtered GZO thin films were investigated using Hall effect measurements (ACCENT, HL5500PC). The optical transmittance and haze measurements were performed using a UV–vis–NIR spectrometer (Jasco, V570). The performance of the a-Si solar cells was measured at 100 mW/cm^2 using an AM 1.5 solar simulator.

3. Results and discussion

Fig. 2 shows SEM surface morphologies of SiO_x buffer layers and bilayer GZO/SiO_x films. The grain size and roughness of the SiO_x buffer layers were found to increase with the argon carrier gas flow rate. Because of a large difference between the main gas and the argon carrier gas flow rate, a vortex was formed inside the plasma-discharging area. The vortex caused radicals to stay in the air for a long time, and this resulted in the formation of particles on the substrates [9]. As the argon carrier gas flow rate increased, the

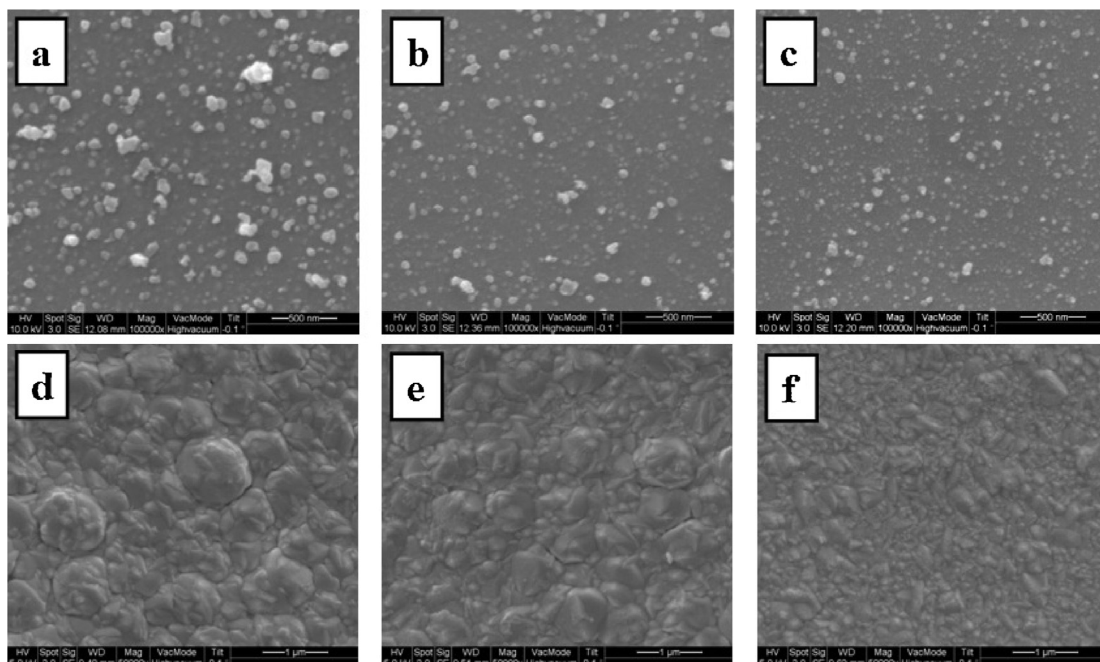

Fig. 2. SEM images of (a) SiO_x (90 sccm) (b) SiO_x (60 sccm) (c) SiO_x (30 sccm) (d) GZO/SiO_x (90 sccm) (e) GZO/SiO_x (60 sccm) (f) GZO/SiO_x (30 sccm).

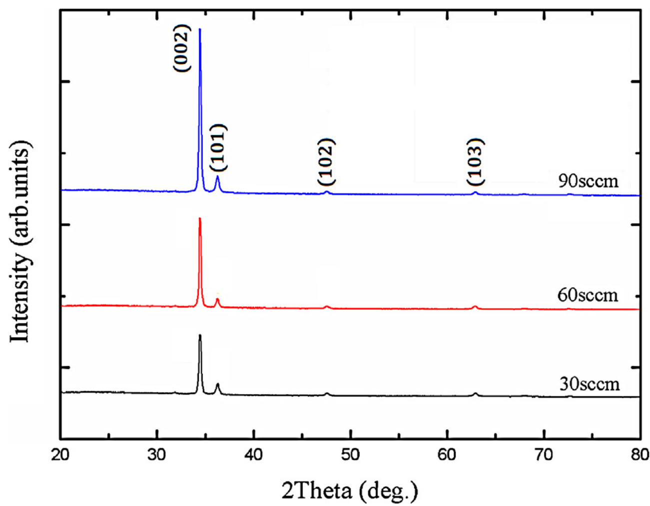

Fig. 3. XRD patterns of GZO thin films deposited on various morphologies of SiO_x buffer layers. The argon carrier gas flow rate of the SiO_x nano-films was set from 30 to 90 sccm.

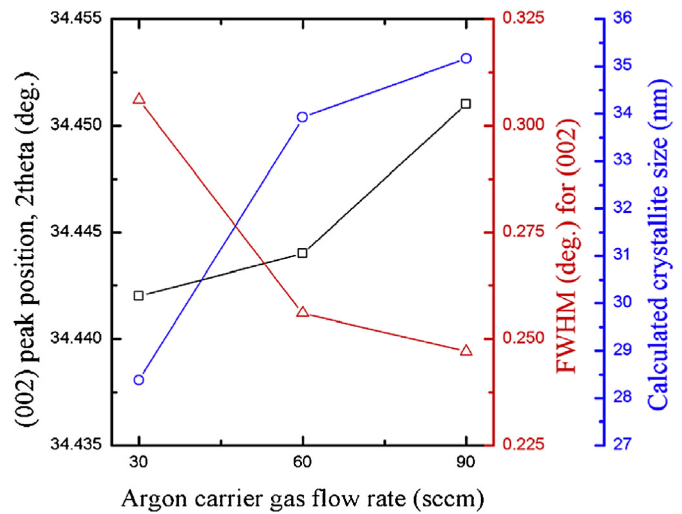

Fig. 4. The diffraction angle of the GZO (0 0 2) peak, FWHM of the GZO (0 0 2) peak and calculated crystallite size along the (0 0 2) orientation for the bilayer GZO films as a function of the argon carrier gas flow rate.

rough surface of the SiO_x buffer layers caused low surface kinetics of the sputtered atoms and a decrease in the nuclei density [10]. Consequently, the bilayer GZO/SiO_x thin films had rough surface microstructure and a large grain size. The 90 sccm sample has the largest root mean square (RMS) roughness of 60.76 nm.

Fig. 3 presents the XRD patterns of dissimilar bilayer GZO/SiO_x thin films. The argon carrier gas flow rate of the SiO_x buffer layers was set from 30 to 90 sccm. XRD patterns of all samples exhibited mainly ZnO (0 0 2) and (1 0 1) diffraction peaks. A strong *c*-axis preferential orientation indicated that the grain growth of the GZO thin film is normal to the plane of the glass substrate. The intensity of the (0 0 2) diffraction peak sharply increased with the argon carrier gas flow rate, meaning that the crystallinity of the bilayer GZO/SiO_x thin films improved.

Fig. 4 shows the diffraction angle, the full width at half maximum (FWHM), and the calculated grain size along the (0 0 2) orientation. The (0 0 2) peak position of all samples is shown to have shifted to a higher Bragg angle compared to that of the standard pattern of ZnO (JCPDS: 36-1451), implying that gallium incorporates into ZnO thin films [11]. This result was consistent with the carrier concentration determined by the Hall measurement, as shown in Table 1. The crystallite size of the GZO thin films

Table 1
Hall effect measurements of non-textured GZO film and bilayer GZO/SiO_x films.

Sample	Resistivity (Ω cm)	Mobility (cm^2/Vs)	Carrier concentration (cm^{-3})
Non-textured	1.10×10^{-3}	23.1	2.448×10^{20}
GZO/SiO_x (30 sccm)	1.35×10^{-3}	27.3	1.694×10^{20}
GZO/SiO_x (60 sccm)	9.72×10^{-4}	28.7	2.238×10^{20}
GZO/SiO_x (90 sccm)	8.98×10^{-4}	29.1	2.387×10^{20}

increased with the surface roughness of the SiO_x thin films. The crystallite size along the (0 0 2) orientation was estimated using the following Debye-Scherrer formula [12]:

$$D = 0.94\lambda/(\beta \cos q)$$

where λ is the wavelength of Cu Kα line, β is the FWHM, and θ is the Bragg diffraction angle. A lower FWHM indicates higher crystallinity. Therefore, the 90 sccm sample had the largest crystallite size because of the lowest FWHM.

The wide-scan XPS spectra of the bilayer GZO/SiO_x films are shown in Fig. 5a. The photoelectronic peaks of Zn, O, C, and Ga were observed. The carbon peak (C1s) was positioned at 285.43 eV

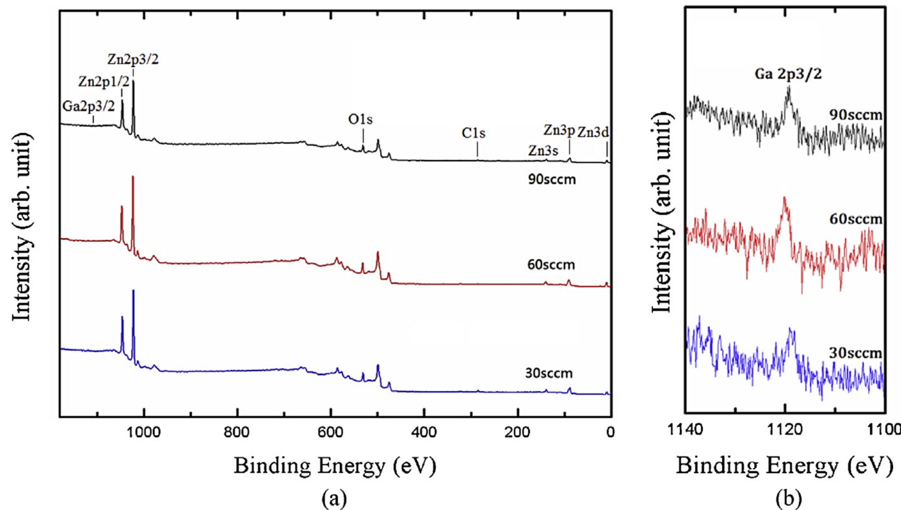

Fig. 5. (a) Wide-scan XPS spectra of the bilayer GZO thin films (b) Ga 2p XPS spectra of the bilayer GZO thin films.

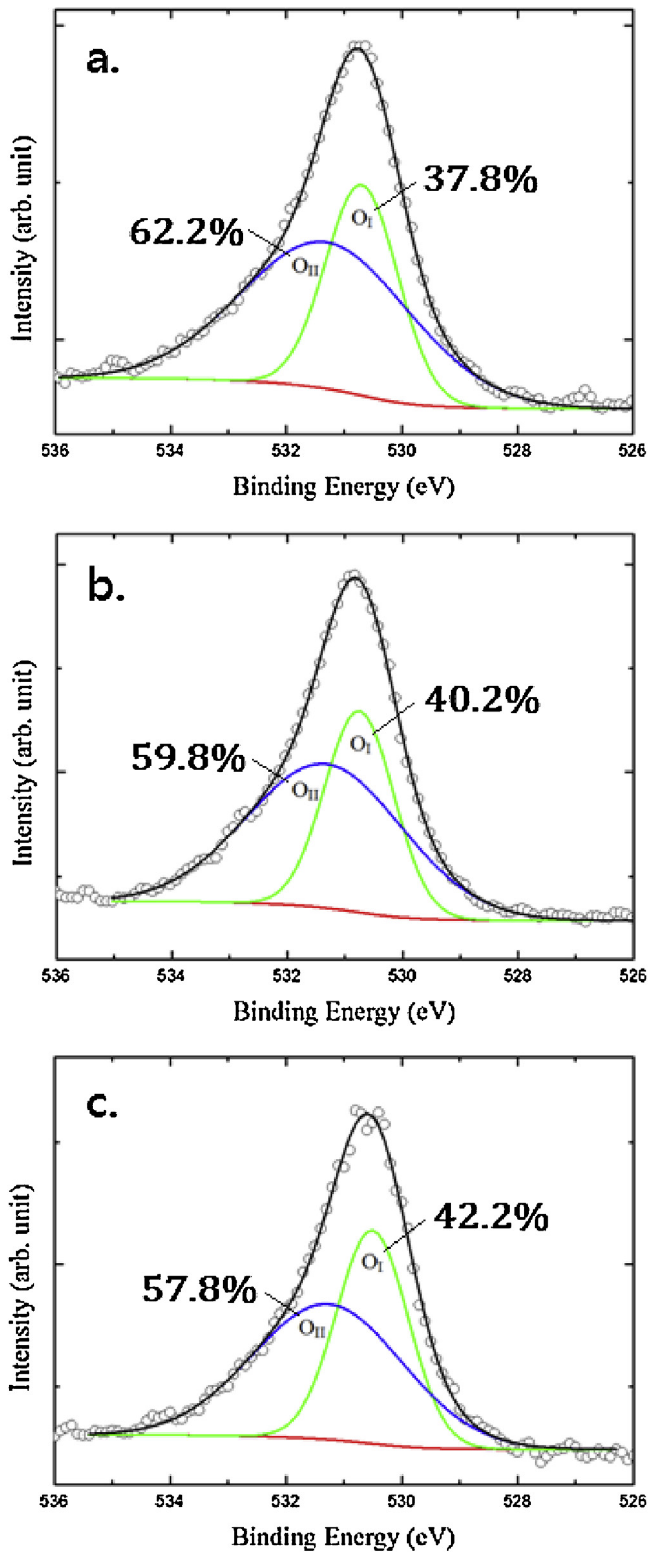

Fig. 6. Narrow-scan XPS spectra of O1s of the bilayer GZO/SiO_x thin films deposited on SiO_x buffer layers with an argon carrier gas flow rate of (a) 30 sccm (b) 60 sccm (c) 90 sccm.

[13]. The carbon contamination may come from sample fabrication and subsequent measurement. No metallic Zn peak was centered at 1021.1 eV [14,15], which confirms that Zn atoms appear only in the oxidized state. Fig. 5b shows the Ga 2p XPS spectra of bilayer GZO/SiO_x films deposited on the SiO_x buffer layers with varied

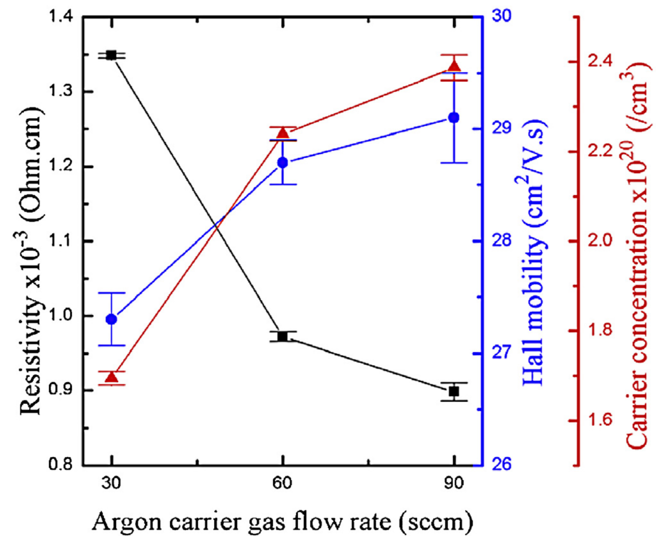

Fig. 7. Electrical properties of the bilayer GZO/SiO_x films as a function of the argon carrier gas flow rate.

argon carrier gas flow rates. The 30 sccm, 60 sccm, and 90 sccm samples have binding energies of Ga 2p3/2 located at 1119.66 eV, 1119.33 eV, and 1118.46 eV, respectively. The result confirms that Ga atoms were incorporated into ZnO films during deposition.

Fig. 6 shows the narrow-scan XPS spectra of O1s of the bilayer GZO/SiO_x films. Before running the XPS measurements, the bilayer GZO/SiO_x thin films were pre-sputtered with Ar plasma to remove surface oxides and contamination. The oxygen spectrum is asymmetric and can be fitted by two Gaussian distributions, located at 530.62 ± 0.11 eV (O_I) and 531.31 ± 0.05 eV (O_{II}). The low binding energy component (O_I) is related to the lattice oxygen of the ZnO (wurtzite) structure, and the high binding energy (O_{II}) component is attributed to oxygen vacancies with the ZnO matrix. The spectra showed that the area percent of O_{II} increased with the argon carrier gas flow rate, implying that GZO thin films deposited on rougher SiO_x buffer layers can lead to an increase of oxygen vacancies (V_o) inside films. Nevertheless, V_o have been reported to act as a deep donor [16–18], and it has not influence on the electrical properties of the GZO thin films.

Electrical properties of the bilayer GZO/SiO_x films as a function of the argon carrier gas flow rate are shown in Fig. 7. Both mobility and carrier concentration increased, which might be attributed to the improvement of the crystallinity of bilayer GZO/SiO_x thin films. The defects inside thin films, such as grain boundaries, vacancies, and interstitials, result in the scattering of the carriers and reduce the carrier concentration. At a high electron density (>10^{20} cm^{-3}), the dominant scattering effect of mobility measured by the Hall equipment was regarded as ionized impurity scattering [19,20]. An enhancement in the crystallinity of the bilayer GZO/SiO_x thin films could reduce ionized impurity scattering, further increasing both the carrier mobility and the carrier concentration. The resistivity of the bilayer GZO/SiO_x films declined, resulting in the achievement of the lowest resistivity (8.98×10^{-4} Ω cm) at the 90 sccm argon carrier gas flow rate. The Hall measurement data of the bilayer GZO/SiO_x and non-textured GZO thin films are summarized in Table 1. The carrier concentrations of all bilayer samples were lower than that of the non-textured GZO thin film. This may be due to unstable oxygen in the SiO_x buffer layers diffusing into the GZO films during 500 °C post-annealing and acting as scattering centers to reduce the carrier concentration.

Fig. 8 shows the optical transmittance and haze of the bilayer GZO/SiO_x films as a function of the argon carrier gas flow rate. All bilayer GZO/SiO_x films exhibited transmittance of more than 80%

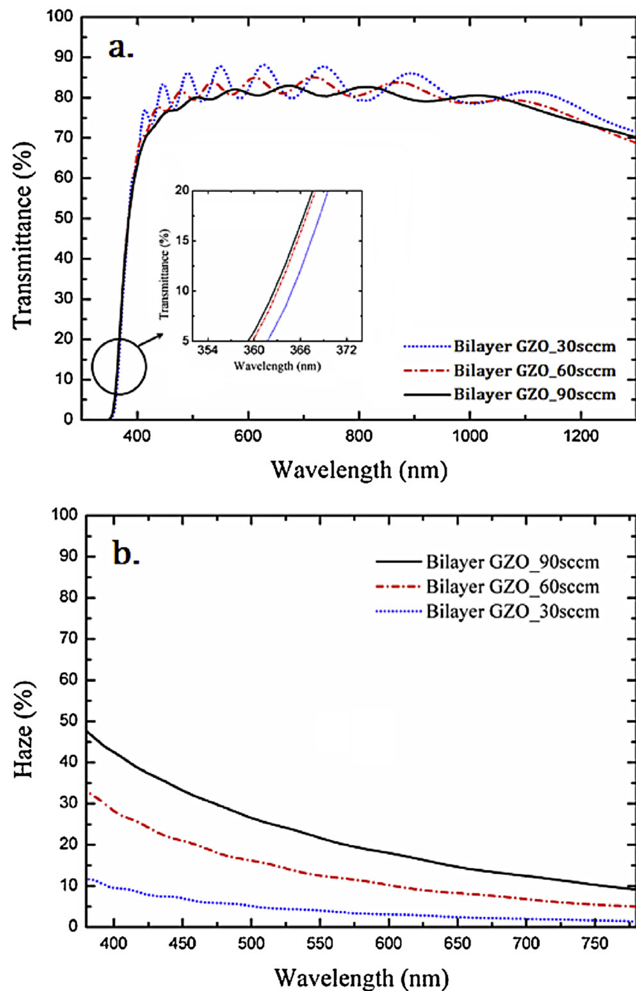

Fig. 8. (a) Transmittance (b) haze of the bilayer GZO/SiO_x films.

Table 2
Comparison of performance for a-Si solar cells with non-textured GZO and textured GZO/SiO_x front contacts.

Sample	V_{oc} (V)	J_{sc} (mA/cm^2)	FF (%)	η (%)
Non-textured	0.710	13.25	58.9	5.55
GZO/SiO_x (90 sccm)	0.849	13.96	57.7	6.85

in the visible region. The inset image presents the magnified curve of the absorption band edge. The blue shifts of the absorption edge occurred as the argon carrier gas flow rate increased from 30 to 90 sccm. This phenomenon is known as the Burstein–Moss effect, which occurs as the carrier concentration exceeds the conduction band edge density of states (DOS) [21–23]. Therefore, the optical band gap of the bilayer GZO/SiO_x films increased (data not shown here) due to an increase in the carrier concentration. With the increase in argon carrier gas flow rate, the bilayer GZO/SiO_x film showed an increase in haze value in the visible region.

The current-voltage parameters for the a-Si solar cells with non-textured GZO and textured GZO/SiO_x (90 sccm) front contacts are shown in Table 2. The conductivity of the bilayer GZO/SiO_x thin film was superior to that of non-textured GZO thin film, and this resulted in a larger V_{oc} [24] because of a decrease in recombination at the front contact/p-type a-Si:H layer interface. The J_{sc} of the solar cell using the bilayer GZO/SiO_x front electrode was higher than that of solar cell using a non-textured GZO front electrode, implying that the bilayer GZO/SiO_x thin film has superior photon collection efficiency to non-textured GZO thin film. An explanation for this is that the bilayer GZO/SiO_x thin film has a higher haze value (22.3%) and a better light-trapping effect compared to a non-textured GZO thin film. The efficiency of the a-Si solar cell using the bilayer GZO/SiO_x front contact was 6.85% and improved by approximately 19% compared with that of the a-Si solar cell using a non-textured GZO front contact.

4. Conclusion

In this study, bilayer GZO/SiO_x and non-textured GZO thin films were deposited on glass substrates by using the APPJ technique and DC magnetron sputtering. Thereafter, a-Si:H layers and GZO/Ag back contact were deposited to complete a-Si solar cells. Roughness of the SiO_x buffer layers deposited using APPJ can be controlled by modifying the argon carrier gas flow rate. Based on the XRD results, the crystallinity of all bilayer GZO/SiO_x thin films improved as the surface roughness of the SiO_x buffer layers increased. Because of the enhancement in crystallinity, both carrier mobility and carrier concentration increased and resulted in a decrease of resistivity. The XPS data confirmed that Ga atoms incorporated into the ZnO films and the V_o number increased with the argon carrier gas flow rate. However, V_o has been reported to act as a deep donor, and it is difficult to contribute the carrier concentration of GZO films. The transmittance of all the bilayer GZO/SiO_x films is more than 80% in the visible region. Rough morphologies of SiO_x thin films resulted in an increment of haze value of the bilayer GZO/SiO_x thin films. The sample of the bilayer GZO/SiO_x (90 sccm) has the highest haze value (22.30%) and the lowest resistivity (8.98×10^{-4} Ω cm), and reaches a maximum cell efficiency of 6.85% (approximately 19% improvement compared to the non-textured GZO sample).

References

[1] L. Prusakova, S. Flickyngerova, M. Fischer, I. Novotny, M. Tijssen, M. Netrvalova, M. Zeman, V. Tvarozek, P. Sutta, Vacuum 86 (2008) 765.
[2] J. Krc, M. Zeman, O. Kluth, F. Smole, M. Topic, Thin solid films 426 (2003) 296.
[3] O. Kluth, B. Rech, L. Houben, S. Wieder, G. Schope, C. Beneking, H. Wagner, A. Loffl, H.W. Schock, Thin solid films 351 (1999) 247.
[4] S.H. Park, J.B. Park, P.K. Song, Current Applied Physics 10 (2010) S488.
[5] V. Assuncao, E. Fortunato, A. Marques, H. Aguas, I. Ferreira, M.E.V. Costa, R. Martins, Thin Solid Films 427 (2003) 401.
[6] K. Sato, Y., Gotoh, Y., Hayashi, K., Adachi, H., Naishimura, Reports Res. Lab Asahi Glass Co., Ltd, vol. 40, 1990, p. 233.
[7] S. Fay, S. Dubail, U. Kroll, J. Meier, Y. Ziegler, A. Shah, Proc. 16th EU PVSEC, Glasgow, 2000, p. p361.
[8] D.W. Kang, S.H. Kuk, K.S. Ji, S.W. Ahn, M.K. Han, Japanese Journal of Applied Physics 49 (2010) 031101.
[9] S.H. Yang, C.H. Liu, C.H. Su, H. Chen, Thin Solid Films 517 (2009) 5284.
[10] B.D. Ahn, Y.G. Ko, S.H. Oh, J.H. Song, H.J. Kim, Thin Solid Films 517 (2009) 6414.
[11] K.M. Chang, S.H. Huang, C.J. Wu, W.L. Lin, W.C. Chen, C.W. Chi, J.W. Lin, C.C. Chang, Thin Solid Films 519 (2011) 5114.
[12] A.R. Babar, P.R. Deshamukh, R.J. Deokate, D. Haranath, C.H. Bhosale, K.Y. Rajpure, Journal of Physics D: Applied Physics 41 (2008) 135404.
[13] W.T. Yen, Y.C. Lin, P.C. Yao, J.H. Ke, Y.L. Chen, Thin Solid Films 518 (2010) 3882.
[14] F. Wu, L. Fang, Y.J. Pan, K. Zhou, Q.L. Huang, C.Y. Kong, Physica E 43 (2010) 228.
[15] S.S. Lin, J.L. Huang, P. Sajgalik, Surface and Coatings Technology 190 (2005) 40.
[16] A. Janotti, Chris G. Van de Walle, Applied Physics Letters 87 (2005) 122102.
[17] X.J. Wang, L.S. Vlasenko, S.J. Pearton3, W.M. Chen, I.A. Buyanova, Journal of Physics D: Applied Physics 42 (2009) 175411.
[18] M.D. McCluskey, S.J. Jokela1, Journal of Applied Physics 106 (2009) 071101.
[19] T. Yamada, H. Makino, N. Yamamoto, T. Yamamoto, Journal of Applied Physics 107 (2010) 123534.
[20] J.J. Robbins, J. Harvey, J. Leaf, C. Fry, C.A. Wolden, Thin Solid Films 473 (2005) 35.
[21] X.Y. Gao, Q.G. Lin, H.L. Feng, Y.F. Liu, J.X. Lu, Thin Solid Films 517 (2009) 4684.
[22] E. Burstein, Physics Review 93 (1954) 632.
[23] S.M. Park, T. Ikegami, K. Ebihara, Thin Solid Films 513 (2006) 90.
[24] Y.C. Lin, T.Y. Chen, L.C. Wang, S.Y. Lien, Journal of The Electrochemical Society 159 (2012) H599.